JOURNAL OF SPACECRAFT AND ROCKETS
Vol. 42, No. 5, September–October 2005

Fluid Structure Interaction on a Generic Body-Flap Model in Hypersonic Flow

Andreas Mack*
DLR, German Aerospace Center, 38108 Brunswick, Germany
and
Roger Schaefer†
DLR, German Aerospace Center, 70569 Stuttgart, Germany

A numerical investigation of a generic reentry vehicle flap configuration at hypersonic speed is presented, which includes considerations of the generic hinge line gap and the outer edges of the flap. Numerical solutions were obtained with a Navier–Stokes code and were coupled via a surface interpolation routine to a structural solver. Two- and three-dimensional solutions were compared for the generic flap model, consisting of a forebody and a body flap deflected 20 deg relative to the forebody with a gap between them. Presented are computational results for a freestream Mach number of 7.3 and an angle of attack of 15 deg with both open- and closed-gap configurations, which are compared to available experimental data. Numerical error, either from the code or the grid, is assessed with the impact of any error on the magnitude of the heat fluxes and the associated gradients. The three-dimensional solutions predict that a strong outflow from the center of the model to the outer edges takes place over the model surface, impacting the flow topology significantly. This was verified with comparison to the experimental results. Temperature peaks predicted by stand-alone computational fluid dynamics solutions were not observed in the experimental data. The investigations confirmed that this is due to strong coupling effects between fluid and structure. Heat conduction into and inside the structure leads to significantly reduced surface temperatures in critical regions.

Nomenclature

l_{Re}	=	Reynolds reference length, m
M	=	Mach number
Pr	=	Prandtl number
$P1$, $P2$	=	pyrometers 1 and 2
p	=	pressure, N/m^2
p_∞	=	far-field pressure, N/m^2
q	=	heat flux, W/m^2
Re	=	Reynolds number
T	=	temperature, K
$T1, \ldots, T4$	=	thermocouple 1, . . . , 4
T_∞	=	far-field temperature, K
w	=	gap width, mm
x	=	x coordinate (flow direction), m
y	=	y coordinate (spanwise direction), m
y^+	=	dimensionless first grid spacing
z	=	z coordinate, m
α	=	angle of attack, deg
γ	=	ratio of specific heats
ε	=	surface emissivity
ρ	=	density, kg/m^3
ρ_∞	=	far-field density, kg/m^3

Introduction

SPACE vehicles reentering the Earth's atmosphere experience high-energy, high-temperature environment that can find ways to seep beneath the outer shielding, the thermal protection system (TPS). In the case of aerodynamic control surfaces, for example, it is difficult to seal completely the gap between the control surface and the configuration. For instance, the body flap of the NASA crew return vehicle, the X-38, was designed conservatively with a complex seal between flap and vehicle to prevent thermal structural damage of the TPS structure and/or the mechanical devices such as actuators and hinges.[1] To make the X-38 body-flap design even more difficult, conduction heating through the relatively thin body flap was expected on top of the convective heating from potential seal breaches. Conduction through the flap would also lead to higher temperatures in the body-flap cove region due to radiative heating from the backside of the body flap to the vehicle surface. The design was done very conservatively due to a lack of accurate heat predictions, such as time-dependent interactions between flowfield and structure during the reentry trajectory. Furthermore, many of those aerothermodynamic problems are difficult to simulate in small-scale wind-tunnel models employing idealized and smooth loft line surface contours and are extremely complex to be fully resolved by computational fluid dynamics (CFD). Today, these local aerothermodynamics become more and more important.

To improve the situation, the DLR, German Aerospace Center, initiated the national program Technologies for Future Space Transportation Systems (TETRA) and the project Integrated Multidisciplinary Design of Hot Structures for Space Vehicles (IMENS). During the TETRA program, the problem of deflected control surfaces with high heating to the outer corners and hinge lines was extensively studied in the DLR arcjet facility L3K.[2] A generic body-flap model was manufactured, consisting of a water-cooled nose and base plate, the forebody, and a 20-deg deflected body flap consisting of C/SiC, with provisions for including various gap configurations at the body-flap hinge line. The gap bottom can be sealed by an aperture with variable slot width (0–5 mm) (Fig. 1). Only the aperture is replaced for different gap configurations; all other components of the model are unchanged. A detailed cross section of the wind tunnel model is shown in Fig. 1, taken from Ref. 2. Two angles of attack, 15 and 30 deg, and a variety of gap sizes, that is, closed, 0.5, 2, and 5 mm, were measured at hypersonic conditions at $M = 7.3$ (Fig. 2). Surface infrared and pyrometer temperature measurements, as well as thermocouples inside the gap, were used.

Received 3 January 2004; accepted for publication 20 August 2004.

*Research Scientist, Department of Spacecraft, Institute of Aerodynamics and Flow Technology, Lilienthalplatz 7.

†Research Scientist, Space Structural Components, Institute of Structures and Design, Pfaffenwaldring 38-40.

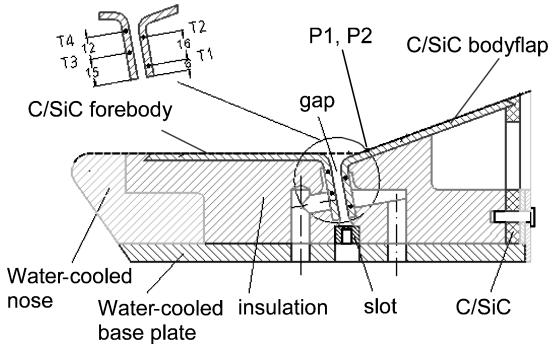

Fig. 1 Cross section of wind-tunnel model.[2]

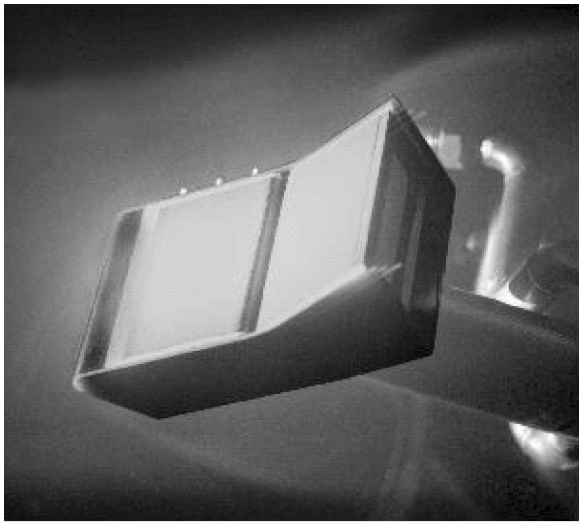

Fig. 2 Generic body-flap model in high-enthalpy flowfield of L3K.[2]

To accomplish the goals of TETRA, CFD solutions of the generic body-flap model were obtained. Based on wind-tunnel observations (infrared temperature distribution images), the computations were completed along a symmetry plane, assuming two-dimensional flow. Also, the calculations assumed perfect gas and nonequilibrium flow, radiation equilibrium wall conditions, and degraded surface cooling in the gap.[3] With the experiments being performed at low Reynolds numbers of 54.000 1/m (laminar flow), neither the open nor the closed gap showed a large separation bubble at the hinge line, whereas the numerical results indicated a very large separation length, resulting in a different flow topology. The computational wall temperatures differed significantly from the experiment, especially for the closed-gap condition, where the gap bottom temperature reached only 400 K for the computations, whereas the experiment indicated 900 K. For the open-gap configuration, the numerical solutions predicted a very large temperature peak at the curvature between the forebody and the gap, which was not observed in the experiments.

One potential source of discrepancy between the computations and the experimental data could be heat conduction effects within the model during the experiments. To investigate this possibility, a numerical coupling tool, which was developed during the IMENS project, based on the DLR Navier–Stokes TAU code, the surface interpolation routine MpCCI, and the structural solver ANSYS, was applied to create a coupled two-dimensional fluid–structure solution.[4] Although that coupled numerical solution showed the expected influences of heat conduction in the gap, that is, an increasing gap temperature, heat conduction effects did not significantly affect the separation length or the overall surface temperatures. Another coupled two-dimensional investigation for this generic body-flap model for non-equilibrium conditions including surface catalytic effects was performed,[5] but, because the gap was not modeled and the structural model included only one C/SiC layer underneath the surface, the results of such an investigation are not considered here.

Whereas the previous numerical investigations mentioned earlier have considered the effects of diverse variables, none addressed the effects of numerical error and crossflow on the flow topology. Therefore, the motivation for the present study is to alleviate the already described poor agreement between experimental and CFD data, by considering the effects of both 1) numerical error of the heat flux prediction either provided by the CFD solver or the grid used and 2) fully three-dimensional calculations.

Experimental Methods

As mentioned before, the experiments were performed in 1999 during the TETRA program. The tests were completed in the arc-heated facility L3K at DLR, Cologne, Germany. The arc heater, with an electrical power of 6 MW, allows testing models up to $280 \times 300 \times 150$ mm in a homogeneous hypersonic high-enthalpy flow. The total enthalpy of the flow was 14 MJ/kg, the mass flow rate 160 g/s, and the Mach number 7.3. To accelerate the flow, a conical nozzle with an half-angle of 12 deg, 29-mm throat diameter, and 300-mm exit diameter is used. As already described, the flow that exits the nozzle is frozen, and almost no chemical reactions take place in the model region. Therefore, the mass fractions in front of and behind the bow shock of the model are the same. The Reynolds number is typically very low, 12.1×10^3 ($l_{Re} = 0.225$ m) in this case. Numerical investigations displayed a boundary-layer thickness at the end of the fore body, indicated by 99.9% of the freestream enthalpy, that is almost one-third the distance to the bow shock. Further experiments with mounted turbulators near the nose of the model could not trigger the laminar boundary layer to become turbulent. Later, these tests were performed at higher Reynolds numbers (200×10^3) for a comparable configuration with the same result. The boundary layer due to this is considered as fully laminar. After achieving a steady-state flow condition, which lasts approximately 100 s, the model is injected into the flow for typically 240 s or longer. At the end of the tests, the surface infrared measurement and the one and two colour pyrometers, P1 and P2 in Fig. 1, have reached steady state, whereas the temperature of the thermocouples inside the gap (T1–T4) were still increasing slightly. This is due to the large thermal capacity of the model because the heat is mainly conducted into the C/SiC plates, but not into the cold insulation parts. Therefore, the temperatures of the thermocouples inside the gap have to be extrapolated to get the steady-state values. The surface infrared data are determined with an emissivity of 0.8 of the C/SiC material and calibrated with the pyrometer measurement points. During the test campaign, a good repeatibility of the tests was documented. Two angles of attack, 15 and 30 deg, and a variety of gap sizes, that is, closed, 0.5, 2, and 5 mm, was measured during the tests. In this paper, only the closed and the fully open gap (5 mm) are considered.

Computational Methods

TAU Code

The TAU code is an unstructured finite volume code developed completely at DLR for the purpose of obtaining an efficient, accurate, and robust Euler/Navier–Stokes solver for subsonic, transonic, and hypersonic flows.[6,7]

The flow calculation algorithm is based on the dual-grid approach, which is well suited to three-dimensional hybrid grids. An edge-based data structure is employed to optimize the flow solver in terms of computer memory requirements and computational performance. The time-accurate three-dimensional Navier–Stokes equations are marched for steady or unsteady conditions by a three-stage Runge–Kutta scheme. Different spacial discretizations (central and upwind) are implemented. The solver includes different upwind schemes, AUSM/Van Leer (see Ref. 8), AUSMDV,[9] and EFM,[10] among others. Perfect gas formulation, equilibrium air, and chemical nonequilibrium are implemented as gas models. State-of-the-art acceleration techniques, such as local time stepping, residual smoothing, and multigrid are used. The viscous terms can be treated as laminar; transitional and turbulent flow are considered with different turbulence

models, such as k–ω or Spallart–Almaras (see Ref. 11). The TAU code consists of three main tools: 1) the preprocessor, which creates the dual grids; 2) the flow solver; and 3) the adaptation tool to refine or redistribute the grids due to specific flow phenomena (pressure gradients, y^+, etc.). When the Navier–Stokes equations are solved for a configuration, different boundary conditions on the surface can be employed, for example, Euler or viscous wall. In this study, the boundary layer will be considered as fully laminar due to the experimental results. Boundary conditions, such as constant wall temperature or radiation equilibrium, are implemented, including catalytic effects. A simple treatment of significantly reduced surface radiation cooling due to surface visibility effects is realized by local emissivities. This approximate estimation is only used for an initial solution, not for the coupled one. In the coupled analysis, the radiation effects are taken into account on the structural side.

In this study, all fluid solutions are performed with perfect gas assumption, using adjusted gas constant R and ratio of specific heats γ. For this, the composition of the gas is taken into account. Initial calculations performed for nonequilibrium conditions[3] displayed no significant differences. Further extensive nonequilibrium calculations during the IMENS project including the nozzle flow of the wind tunnel, as well as calculations for a generic forebody-model, confirmed this. The flow that exits the nozzle of the wind tunnel is strongly frozen. Oxygen (O_2) is completely dissociated, whereas nitrogene (N_2) just started to dissociate. All chemical effects mainly take place in the arc heater or on the way through the nozzle, whereas the model faces a frozen flow. The stagnation temperature on the model cannot force further chemical reactions due to the low density of the mixture combined with a small bow shock distance from the surface (some millimeters), which means very small relaxation lengths. Only a fully catalytic wall shows a significant increase in temperature due to the change in the gas mixture near the wall (approximately 200 K). However, because the C/SiC material shows quasi-noncatalytic properties, this effect is neglected. Therefore, the difference between a perfect gas solution and a nonequilibrium solution is very small (maximum of 30 K in temperature).

ANSYS Code

The ANSYS code is a commercial software tool for analyzing structural behavior due to mechanical and thermal loads. It follows a finite element method- (FEM-) based approach to treat, for example, the stresses or thermal distributions due to surface loads. An attribute of ANSYS is that all tools for a full workaround, such as preprocessor for creating the models, different structural solvers (thermal, structural, etc.), and the postprocessing tool, are included. It can be run in interactive or batch mode on many platforms from personal computers to high-performance computers. It is also possible to run time-accurate solutions. The structural meshes in this work have been created as quasi-structured ones (hexaedrons) to take advantage of the cell shape along the sharp edges for coupling. This regular shape helps to minimize the interpolation error of the surface loads because the structural surface meshes are usually coarser than the fluid meshes. The computations in this study are always done for steady-state solutions. An important tool concerning this work is the radiation module. There, the surface radiation matrix is calculated taking into account second-order visibility effects. That means that for every surface panel the visibility to all other surface panels is calculated. Radiation of all other panels, as well as one reflection of the emitted energy of the own panel, is taken into account. By this, degraded radiation cooling, for example, in gaps or on body-flap leesides, can be treated accurately. Because the model investigated here is rigid, thermally driven deformations have been neglected.

Coupling Strategy

The coupling strategy used here is shown in Fig. 3. In the loose coupling approach, the CFD solver TAU calculates the surface heat flux and pressure, which has to be interpolated to the surface mesh of the structural solver, ANSYS. Taking this as the boundary condition, the structural solver performs a thermal analysis and calculates

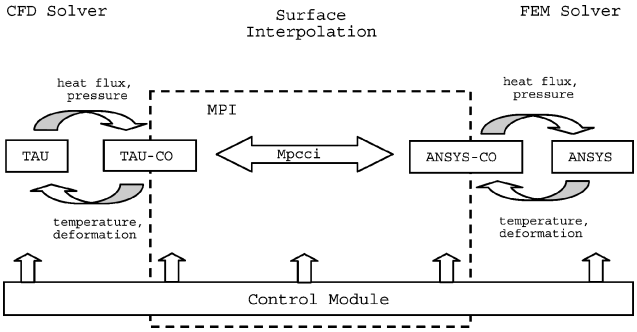

Fig. 3 Coupling strategy for fluid–structure interaction.

a new temperature distribution inside the structure and the deformation (not considered here) due to aerothermodynamic (thermal and pressure) loads. Relaxation of the aerothermodynamic loads can be applied to improve robustness if necessary.

Surface temperature and displacements of the coupling surface are interpolated back to the CFD code. Coupling iterations are performed until convergence is reached, for the simulations presented here, typically 3–5 iterations. Fluid and structural solvers are started by so-called coprocesses. This allows running jobs in a batch mode and minimizes the active time in machine for each solver. Also this strategy, different CFD and FEM codes without internal interface to the interpolation routine can be used. The surface interpolation is done with the commercial surface interpolation software MpCCI,[12] described next. Coprocesses, interpolation, and the control module run in parallel mode, and the CFD and FEM code are started sequentially by the coprocesses.

Surface Interpolation Routine MpCCI

The design of the commercial MpCCI interpolation routine[12] was done to create an interpolation tool that easily can be used for different types of code, preserving the functionalities completely. The implementation is done for loose coupling by the surface interpolation technique. There are nonconservative and conservative, for example, for fluxes, interpolation routines for matching or nonmatching grids, for example, structured to unstructured grids, implemented. An efficient neighborhood search with different algorithms, also as parallel environment, is available. The applications are linked by message-passing interface (MPI), so that a parallel or sequential distributed execution is possible. The tool has a good portability to many architectures. The interfaces of the coupling codes to the MpCCI can be directly implemented in the coupling codes, with only a few new functions that are linked with the MpCCI libraries to the code. If the sources of the code are not available, for example, for commercial products such as ANSYS, coprocesses have to be written. These processes run in the MPI environment as parallel processes that just read in or write out files that can be used by the structural or fluid codes and that start these codes in sequential mode.

Numerical Accuracy

Grid Refinement Study

To check the grid dependency of the fluid solution, a grid convergence study was done for both the two-dimensional and three-dimensional cases. In two dimensions, on three different meshes, coarse, medium, and fine, the calculations are performed with 12, 24, and 48 points in wall normal direction in the structured layer of constant thickness. During the adaptations, mainly the unstructured part was modified. The structured part was conserved in the wall-normal direction. The number of adaptations necessary before reaching convergence depends on the mesh and the status of the gap, closed or open (Table 1). The coarser the mesh, the more adaptations are necessary to achieve a converged solution. On a finer mesh, the phenomena are already present more accurately before the first adaptation. Indeed, the number of points is increased by a factor of 3 (or 2 in the case of the open gap), by 2 for the medium mesh, and

Table 1 Mesh sizes of adapted and initial meshes

	Closed gap			Open gap		
Mesh	No. of adaptations	Final mesh no. of adaptations	Initial mesh no. of points	No. of adaptations	Final mesh no. of adaptations	Initial mesh no. of points
Coarse	7	36,000	11,600	5	21,400	11,600
Medium	5	72,000	34,000	5	77,500	34,000
Fine	4	150,000	100,800	3	138,000	100,800

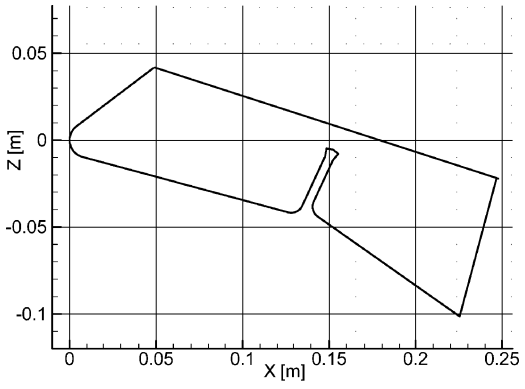

Fig. 4 Model-geometry outline with coordinate system.

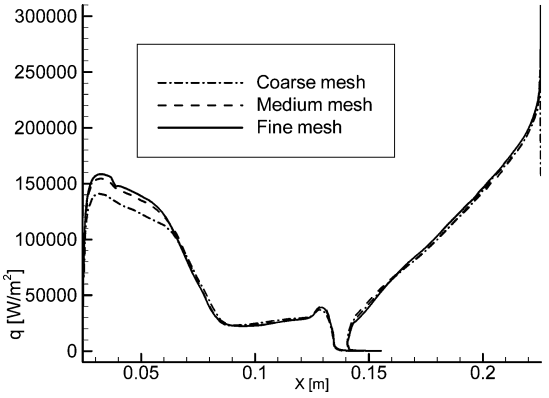

Fig. 5 Closed gap: grid convergence heat flux.

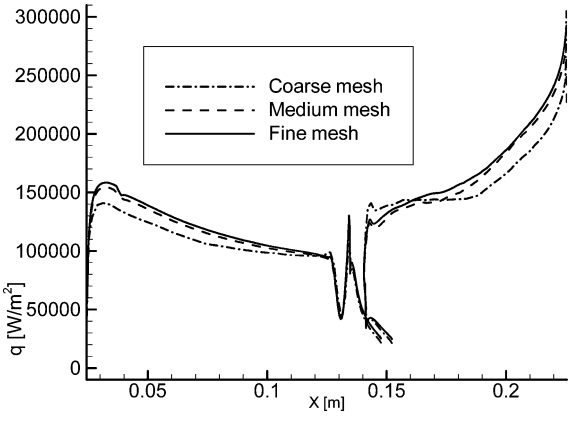

Fig. 6 Open gap: grid convergence heat flux.

by 1.5 for the fine mesh. Such adaptations have a direct influence on the accuracy of the result as follows.

A global coordinate system with the generic configuration used for the numerical investigations is in Fig. 4. Heat fluxes obtained with the three final meshes (coarse, medium, and fine) are shown for both cases (closed and open gap), in Figs. 5 and 6, respectively. The separation zone (open-gap configuration) moves slightly forward with a finer mesh because of the more accurate gradient detection

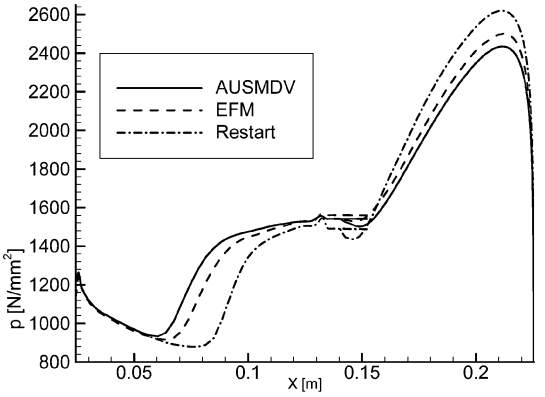

Fig. 7 Closed gap: scheme dissipation influence on surface pressure.

and a better resolution on these meshes. For all meshes, the y^+ are well below 0.5.

The difference of the solutions between the medium and the fine mesh is small. Grid convergence was not reached completely, but all gradients are well predicted and further refinements in two dimensions would not change the flow features qualitatively.

Numerical Dissipation Study

To examine numerical dissipation effects, the following investigation was performed. Two calculations are made on the same grid (medium grid with closed gap) with two different schemes: AUSMDV[9] and EFM[10] (Fig. 7). The EFM scheme, due the numerical scheme employed, is more dissipative. Different results of the solvers, therefore, can be interpreted as a variation of the numerical dissipation. The restart corresponds to a nonconverged state (separation not fully developed). The two solutions, one for AUSMDV and one for EFM, correspond to a converged solutions. The results of the more dissipative solver, the EFM in this case, presents a smaller separation length (Fig. 7). The same observation can be done with a low-order solver compared to the second-order solver used here or even higher-order schemes (not shown here).

Results and Discussion

Two-Dimensional Numerical CFD Investigations

In the following sections, a brief description of the flow features for the two-dimensional configurations will be given to obtain an overview of the characteristics for gap flow phenomena for this generic model. The adjusted flow conditions for perfect gas to match the frozen onflow are listed in Table 2.

Closed Gap

Figure 8 shows the adapted mesh for the closed-gap configuration. Closed gap means that the gap is a cavity closed at the bottom without any outflow. Because the grid has been adapted to the flow phenomena, the bow shock, the separation, and the body-flap shocks can be observed by the clustering of the mesh. At the nose, the flow passes quickly from freestream conditions to the stagnation conditions. About midway back on the forebody, a separation shock is observed, induced by the pressure increase from the deflected body flap. Also, a large separation bubble is evident over the gap region, whereas on the body flap, a shock is observed.

Table 2 Flow conditions

Parameter	Value
M	7.27
α	15 deg
T_∞	620 K
p_∞	89 Pa
ρ_∞	0.000402 kg/m^3
Re	1.21×10^4
l_{Re}	0.2247 m
R	358.43
γ	1.455
Pr	0.72

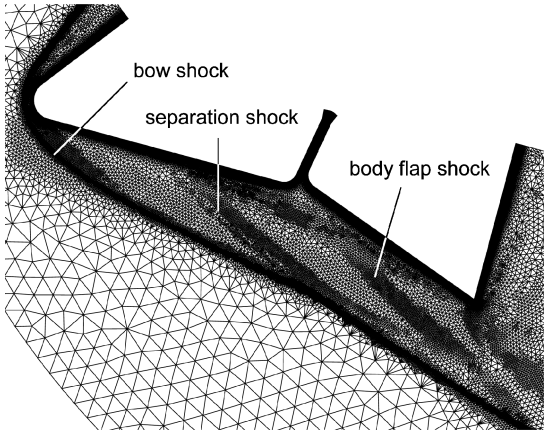

Fig. 8 Closed gap: adapted flowfield grid.

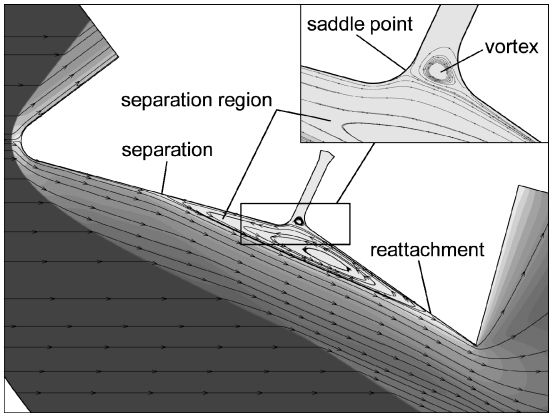

Fig. 9 Closed gap: flowfield topology.

Figure 9 shows the streamlines along the symmetry plane. The streamlines in the gap zone (Fig. 9) show the separation zone and a vortex in the gap entrance. The reverse flow over the main part of forebody and body flap separates the outer flow from the slowly rotating flow in the gap region. These phenomena are also visible in the temperature (Fig. 10) and heat flux (Fig. 11) distributions. Temperature increases rapidly from the cooled nose temperature in the insulation part to 1320 K (starting from $x = 0.025$). Then, due to the difference of emissivity between the insulation, it increases once again to 1350 K on the C/SiC plate ($x = 0.04$). Inside the separation bubble, there is a decrease of the temperature, to 840 K ($x = 0.09$). Because of the small Mach number, this leads to a lower skin friction and temperature and, therefore, reduced heat fluxes. Just in front of the gap, there is a slight increase of the temperature (965 K, $x = 0.13$) because of a saddle point in the reverse flow zone. The stagnation in this zone increases the temperature. At the gap bottom, the temperature reaches less than 400 K and the heat flux vanishes (Fig. 11). On the body flap, the temperature keeps increasing until a value of approximately 1600 K at the trailing edge.

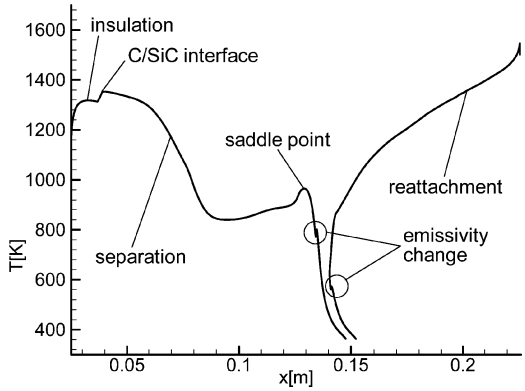

Fig. 10 Closed gap: surface temperature.

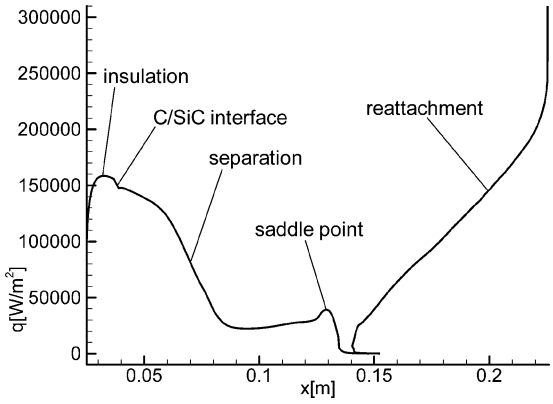

Fig. 11 Closed gap: surface heat flux.

Inside the gap, local temperature peaks appear at each gap side (Fig. 10). They are due to the change of emissivity between the walls of the gap ($\varepsilon = 0.2$) and the others ($\varepsilon = 0.8$), which approximates the degraded radiation cooling due to visibility effects of the gap walls. However, because of the low temperature in this area, this has no significant effect.

Open Gap

For the open-gap case, the aperture at the gap bottom is completely removed, leading to a slot width of 5 mm with a strong outflow. The freestream conditions are exactly the same as the closed-gap case (Table 2). The gap bottom boundary condition is not treated as an impermeable wall but as outflow; compare the closed gap case. Numerical investigations showed that the pressure at the gap exit during the experiment was low enough to reach supersonic speed at the gap exit.

There is no change of the flowfield in the nose region because this zone only depends on the freestream conditions (Fig. 12). Compared with Fig. 3, for the open gap, only the bow and body-flap shock can be seen on the mesh. The separation shrinks to the gap entrance forward wall, as plotted in Fig. 13. These streamlines indicate how part of the flow is directed into the gap. Compared to the closed-gap configuration, only a small separation occurs.

Once again, temperature and heat flux show the same behavior on the front part of the forebody as for the closed gap case (Figs. 14 and 10). Without large separation, temperature slowly decreases from 1350 ($x = 0.04$) to 1200 K until the gap entrance ($x = 0.128$). The decrease of temperature in front of the gap, also visible on the heat flux curve (Fig. 15), corresponds to the location of the main separation. After that, the peak of temperature and heat flux can be explained by the local reattachment of the flow (visible in Fig. 14 and 15) inside the gap on the forward wall. This point is the critical one, with the highest overall temperature of 1650 K ($x = 0.0135$). Finally, the last minimum and maximum peaks of temperature and heat flux on the gap backward wall are due to the expanding flow at the

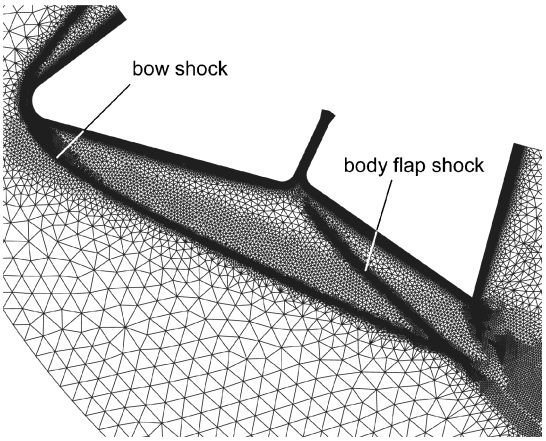

Fig. 12 Open gap: adapted flowfield grid.

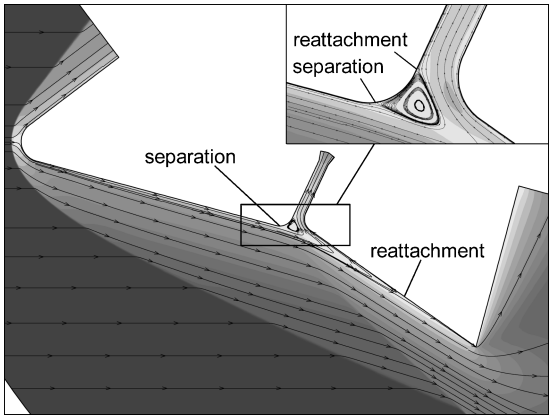

Fig. 13 Open gap: flowfield topology.

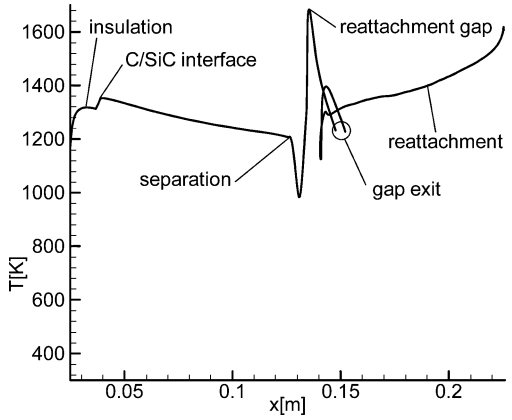

Fig. 14 Open gap: surface temperature.

curvature between the gap and body flap. The body-flap temperature increases from 1300 on the gap curvature to 1600 K at the trailing edge.

Three-Dimensional Numerical CFD Investigations

For three-dimensional calculations, two meshes are generated, a coarse (12-prism layers) and a medium one (24-prism layers). Points distributions are comparable to the two-dimensional grids, whereas the surface is discretized with triangular cells. Local grid refinement on the surface is necessary to obtain a good solution around the sharp edges. The meshes were adapted several times to achieve boundary-layer and shock resolutions comparable to the two-dimensional results. Because of the increasing number of grid points in three dimensions, the grid convergence study in three dimensions was based on the two-dimensional results to confirm them for three-dimensional flow. Meshes with 12 and 24 points inside the structured layer were generated, and the overall thickness of this layer was reduced. By this procedure, the wall-normal point distribution was further refined. The meshes showed improvements in heat flux predictions comparable to the two-dimensional meshes (not shown here).

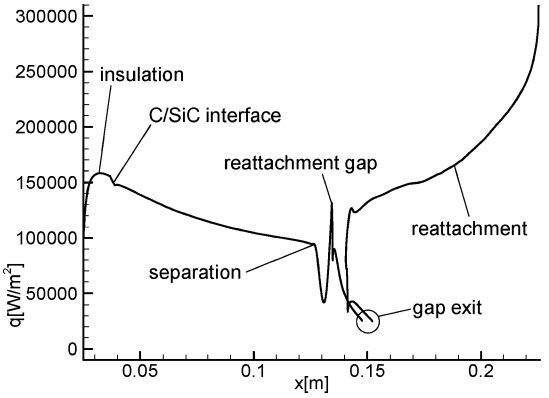

Fig. 15 Open gap: surface heat flux.

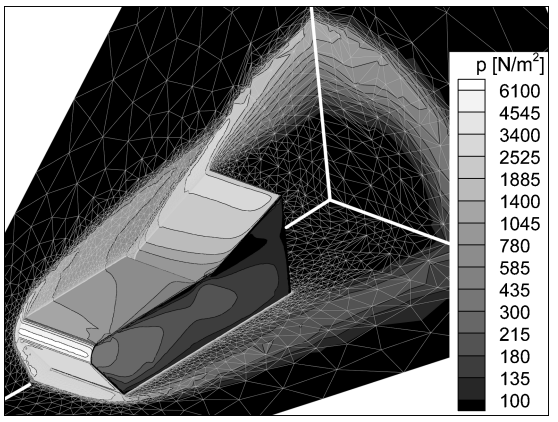

Fig. 16 Three-dimensional flow topology: pressure distribution on surface and far field.

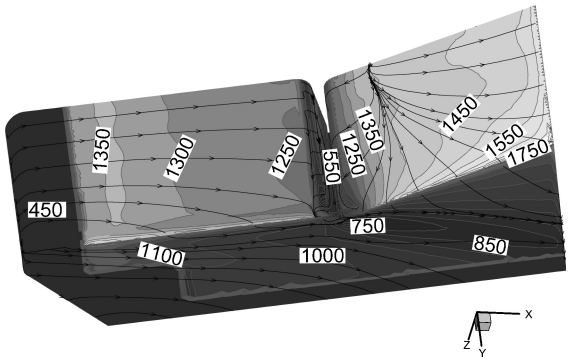

Fig. 17 Closed gap: surface streamlines and temperature distribution.

Closed Gap

The main difference between the two- and the three-dimensional models is the crossflow. Although the pressure distribution on the body flap (Fig. 16) does not vary strongly in spanwise direction, there is a strong influence of the crossflow. This effect can also be clearly seen in Fig. 17, where the streamlines near the symmetry plane stay in the x–z plane, but the ones near the edge of the model tend to exit by the side. The air that enters the gap does not stay inside but is evacuated in the crosswise direction, along the gap,

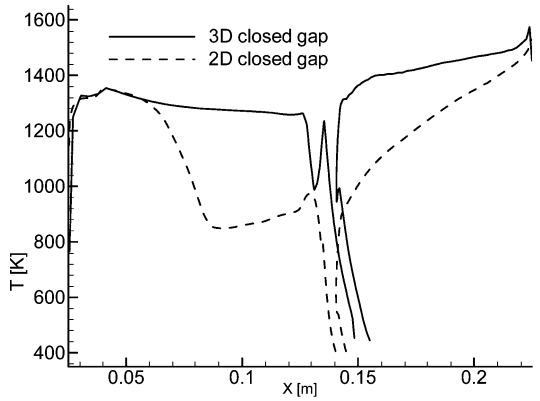

Fig. 18 Closed gap: comparison of surface temperature in symmetry plane, two and three dimensional results.

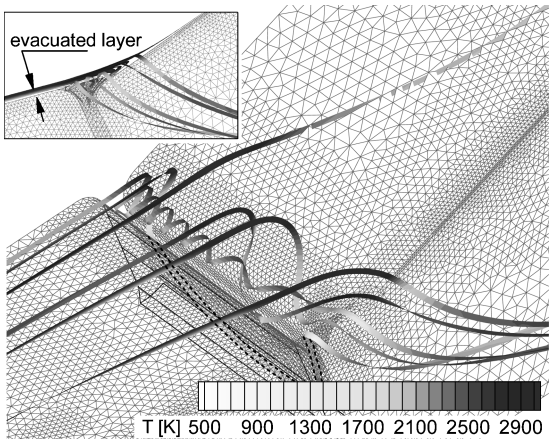

Fig. 19 Closed-gap flow phenomena: evacuated streamlines carrying temperature distribution.

toward the lateral edge of the model, generating a cold spot at the side plate of the gap.

Compared to the two-dimensional results, there is no separation on the forebody (Fig. 18). The three-dimensional relief of the flow within the closed gap allows the separation zone to shrink. The separation line on the forebody is now located at the gap entrance, whereas the reattachment line on the body flap moves closer to the gap. The flow on the forebody appears relatively two-dimensional; however, the body flap is highly three-dimensional. Temperature on the body flap in the portion of the gap affected by the flow separation is lower than the temperature on the remaining parts. Finally, the streamlines on the side of the model diverge behind the gap because of the exiting air. Figure 19 gives a closer look at this gap flow phenomenon. Streamlines with temperature scale show the effect of the spanwise open separation. When separating from the forebody at the gap entrance at 1300 K, streamlines are passing by the gap bottom, cooling down to 500 K, or form vortices at the gap entrance leading to a reattachment line on the gap forward wall (also Fig. 18) and exit in spanwise direction. Because the separation is open, the lower boundary layer of the forebody is evacuated into the gap (Fig. 19 inset). Flow that passes over this layer attaches on the body flap. Therefore, the reattachment streamline is not comparable with the two-dimensional case, because this streamline comes out of the hot boundary layer some distance from the surface. Because of this, temperature at the reattachment line in the three-dimensional case is much higher than in the two-dimensional case in addition to the reattachment line moving forward (Fig. 18).

Figure 20 shows the slices made in the three-dimensional model to extract temperature and heat flux for visualization. In the spanwise direction, the temperature (Fig. 21) does not vary much for the forebody. In the vicinity of the gap and on the body flap, a strong crossflow is present. The heat flux variation is very important near the lateral edge ($y = -0.0015$ and -0.005) because of the crossflow. In these sections, the effects of a spanwise insulation part ($y = -0.005$) between forebody/body flap and sideplate and the three-dimensional flow around the side edge ($y = -0.0015$) are superposed. Temperature decreases because of an increasing emissivity ($\varepsilon = 0.95$ on insulation compared to 0.8 on C/SiC). This can be seen at the temperature distribution, where the temperature at the $y = -0.05$ section does not reach 1360 K at the front of the forebody ($x = 0.04$) as in all other sections. There is a lower temperature level, comparable to the insulation, between cooled nose and forebody. Near the side edge ($y = -0.0015$), temperature and heat flux rise significantly. On the gap forward wall, the reattachment can be seen due to an increase of temperature and heat flux. On the forebody along the y axis, the heat flux is almost constant (Fig. 22), except for a small peak at the edge because of the edge flow. In the gap region, the heat flux is very low, but slightly higher than in the two-dimensional case due to the gap flow described earlier.

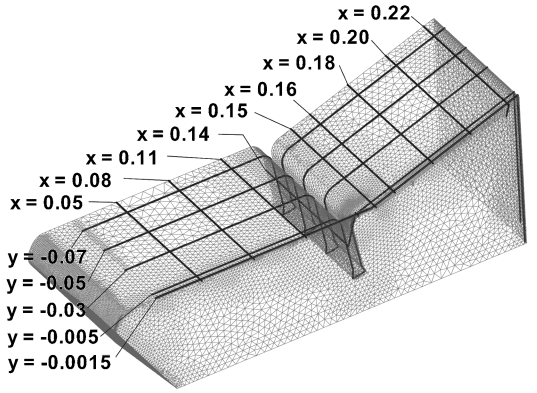

Fig. 20 Three-dimensional surface grid: slices for data extraction.

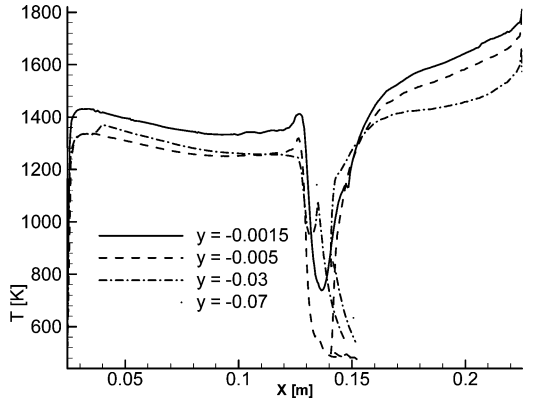

Fig. 21 Closed gap: surface temperature distribution along x axis.

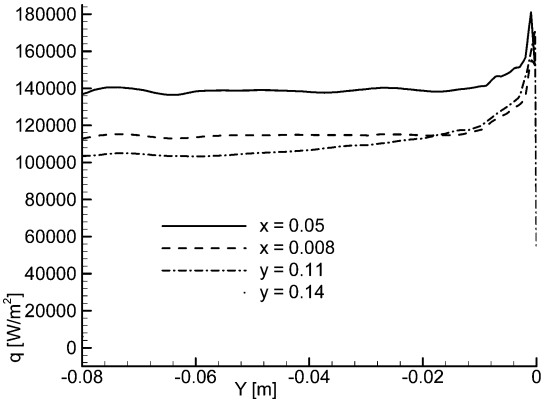

Fig. 22 Closed gap: heat flux along y axis on forebody.

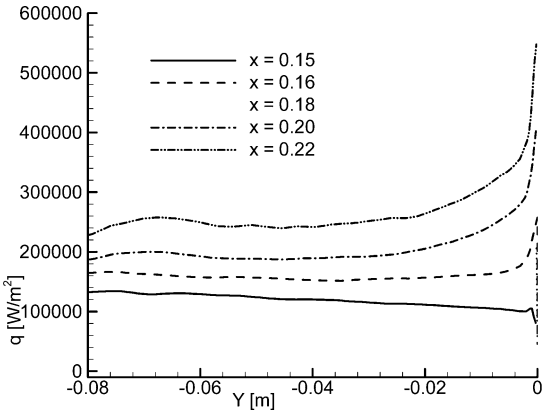

Fig. 23 Closed gap: heat flux along *y* axis on body flap.

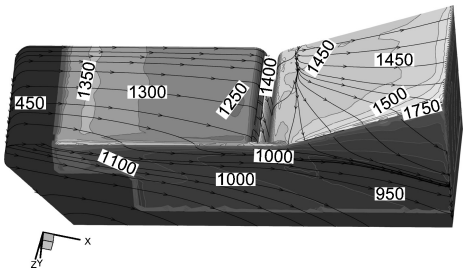

Fig. 24 Open gap: surface streamlines and temperature distribution.

On the body flap, the three-dimensional effect on temperature and heat flux in the spanwise direction is stronger than on the forebody (Fig. 23), and the absolute values are higher because of the deflected flap and the strong crossflow effect downstream of the gap. Values are higher near the side edge and trailing edge. At $x = 0.15$, the heat flux and the temperature, especially at the side edge, are low because of the separated flow there.

Open Gap

The temperature distribution on the forebody of the open-gap configuration is identical to the one for the closed-gap configuration (Fig. 24 compared with Fig. 17). Because there is a strong flow through the open gap, there is no longer a lateral exiting stream at the gap side. Consequently, there is no cold spot in that zone, but a hot spot due to the saddle area. In contrast to the closed-gap model, the streamlines at the side of the model do not diverge, which shows the absence of spanwise out going flow from the gap. Once again, the trailing and side edges of the body flap are hotter than the remaining part, especially the trailing edge. The reattachment at the body flap (zone where the flow is split between the stream continuing to the trailing edge and the stream going to the gap) is now much closer to the gap, and therefore, the temperatures after reattaching the body flap are much higher than in the two-dimensional results (Fig. 25). Reattachment on the body flap moved closer to the gap; by this, the mass flow through the gap is reduced. Therefore, the temperatures inside the gap are below that in the two-dimensional case: on the one hand, at the gap reattachment peak (from 1650 in two dimensions to 1500 K), on the other hand, the temperature in the gap bottom (from 1200 in two dimensions to 1000 K) (Fig. 25). There is a separation line on the front gap curvature because the stream going down the gap is facing a large pressure increase at the corner arc.

The spanwise sections of temperature (Fig. 26) and heat flux (not shown here) show that both are higher at the body flap than at the forebody. At the reattachment, maxima appear that lead to almost constant distributions on the body flap except the edge effects. Heat flux and temperature peaks on the edge of the body flap and the gap forward wall occur. Temperature at the gap exit remains at 1000 K except at the section for $y = -0.005$, where it drops to 600 K (insulation, internal edge flow).

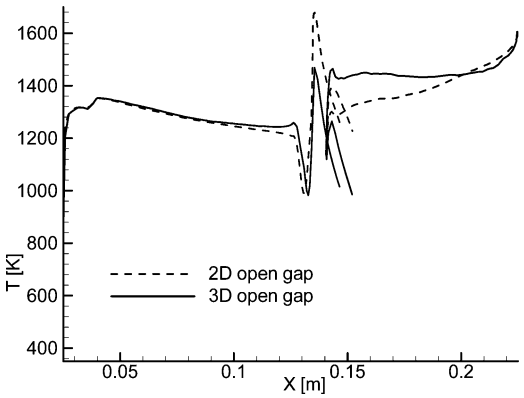

Fig. 25 Open gap: comparison of surface temperature in symmetry plane, two- and three-dimensional results.

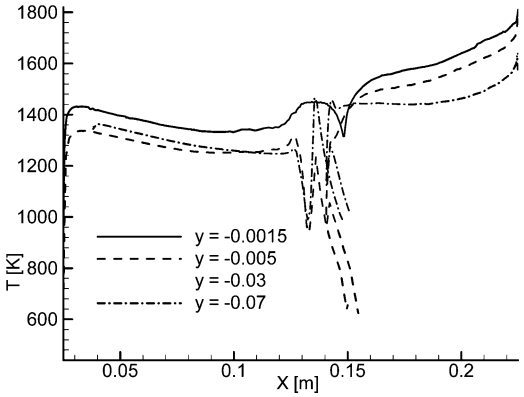

Fig. 26 Open gap: surface temperature distribution along *x* axis.

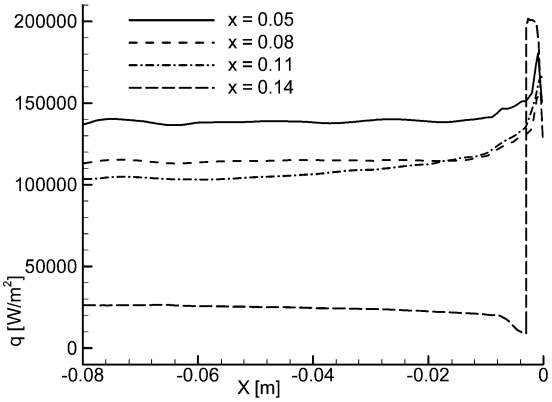

Fig. 27 Open gap: heat flux along *y* axis on fore body.

In the crosswise direction, the heat flux (Fig. 27) distributions at the forebody are similar to the closed-gap distributions except on the gap forward wall ($x = 0.14$). Inside the gap, the temperature is higher (1200 K compared to 400–800 K) as well as the heat flux, due to the strong flow passing through the gap. The temperature at the gap side plate (section at $x = 0.14$, $y = -0.002$), not shown here, increases locally to 1600 K, displaying the high heat flux saddle point area there. On the body flap, the peak of temperature and heat flux (Fig. 28) at the side edge is observed as a three-dimensional effect, comparable to the closed-gap configuration. This peak is very strong for $x = 0.22$ (near the trailing edge).

Comment on Three-Dimensional Configuration

When the open-gap configuration is compared with closed-gap configuration, there is not much difference in the overall flow topology as in the two-dimensional results: Both cases have separating flow on the forebody just in front of the gap and reattachment on

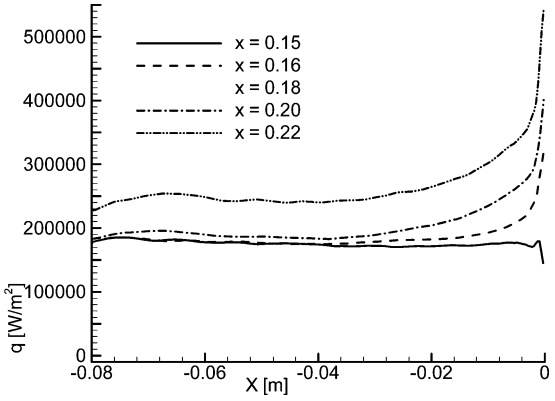

Fig. 28 Open gap: heat flux along *y* axis on body flap.

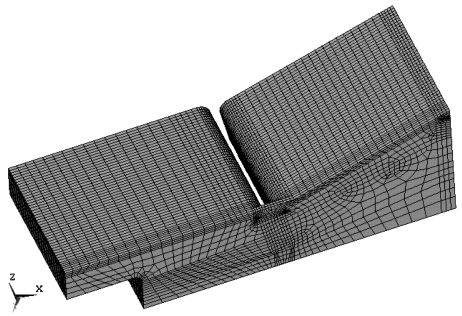

Fig. 29 Structural model (ANSYS) with removed nose part.

the body flap. On the gap forward wall, reattachment leads to an increase of temperature and heat flux. This topology is driven by exiting gap flow. In one case (closed gap) the gap flow is exiting in the spanwise direction and in the other (open gap) by the gap bottom. Only inside the gap, there is strong hot flow at sonic speed for the open gap compared to cold flow at low Mach number for the closed gap. Therefore, the three-dimensional calculation is the key to better understanding of this experiment.

Fluid–Structure Interaction

Structural ANSYS Model

For all simulations, the same structural model generated with ANSYS is used. All components relevant for thermal analysis, such as the C/SiC TPS–structure, as well as insulation or cooled base plate, were applied according to the experimental model in Fig. 29. The cooled nose and base plate were modeled as a boundary condition with constant wall temperature because these parts are water cooled and made out of copper or stainless steel, respectively. Meshing was performed using a three-dimensional eight-node finite element type model with one degree of freedom, temperature, at each node. Therefore, the mesh was created in a quasistructured way. This method obtains well-shaped hexahedron cells along the edges of the model that face high heat fluxes. The material properties were considered as nonlinear, according to the real behavior. The C/SiC material, for example, is highly orthotropic concerning heat conductivity. In the wall-parallel direction, the heat conductivity is much higher than in wall-normal direction due to the embedded fibers orientation. Radiation cooling into space as well as degraded surface radiation due to visibility effects are also considered in the model as described earlier. The thermal analysis is performed for steady state; surface pressure load and deformation are neglected because they are not relevant for these tests due to a rigid model and model holder.

Closed-Gap Configuration Simulation

The first coupling results have been performed on the coarse meshes due to computing time. Previous two-dimensional coupled results of this generic configuration are shown and discussed in Ref. 13.

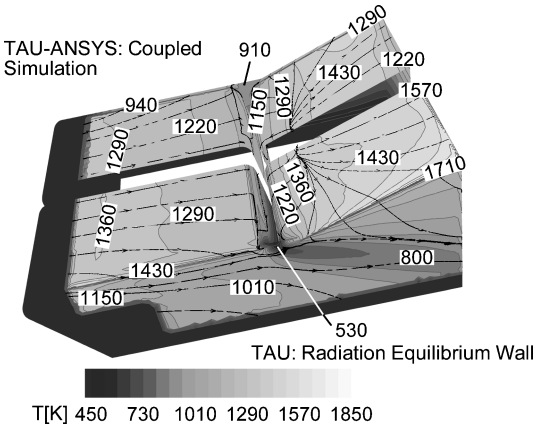

Fig. 30 Closed gap, coupled and uncoupled solutions: surface streamlines and temperature distributions.

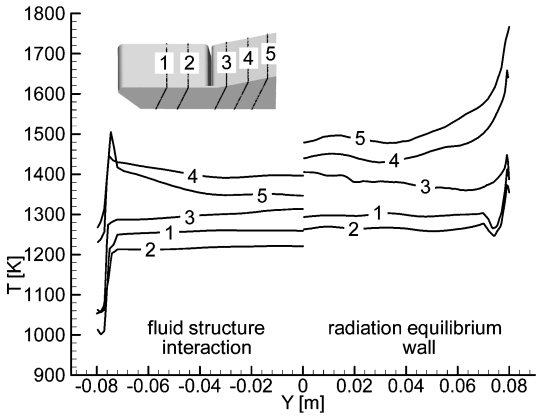

Fig. 31 Closed gap: comparison of coupled and uncoupled solution along *y* axis.

The coupled analysis has little influence on the flow topology, as shown in the streamlines of Fig. 30. The surface temperature distribution of the coupled fluid–structural solver result is smoother than the temperature of the fluid code results. The heat from hot regions has been conducted inside the material of the model to cooler regions. All side edges become cooler; the maxima of temperature occur now at the forebody and the body-flap C/SiC elements. The orthotropic heat conductivity behavior with increased conductivity in wall parallel direction and the laterally mounted side and back walls impinged with the high heat flux peaks reduce the temperature load significantly by several hundred Kelvin (Figs. 31 and 32). The main surface gradients of the experiment are well predicted with the coupled solution. The first two experimental points on the forebody, almost 1600 and 1500 K, are too high because of an optical error. Particles of Al_2O_3 or SiO_2 were washed out from the insulation material and, with their different emissivity, lead to too high values. Finite catalytic effects of the C/CSiC surface may also cause a slight increase of surface temperature. Numerical investigations (not shown here) for fully catalytic wall boundary conditions in nonequilibrium flow displayed an increasing surface temperature of 200 K. However, until now, no reliable data for the material properties concerning catalytic effects have been available; therefore, this effect is not further considered here. Because the fluid solution is based on a perfect gas assumption, there is minor uncertainty in the temperature level as described before. The high thermal loads around the lateral edges have disappeared because of the higher heat conduction of the C/SiC side plates, which transfer the heat to the base plate. In particular, the trailing edge cools off due to strong internal heat convection to the backside wall of the model, which is heated and radiates strongly. In the results in Fig. 33, the cooled trailing edge can be seen, as well as the significantly heated gap walls that reach 1000 K. The energy is transferred from forebody and body flap; therefore, the coupled surface temperature is 50 K

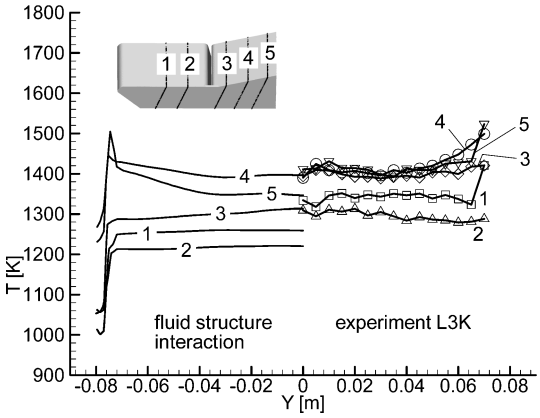

Fig. 32 Closed gap: comparison of numerical and experimental solution along *y* axis.

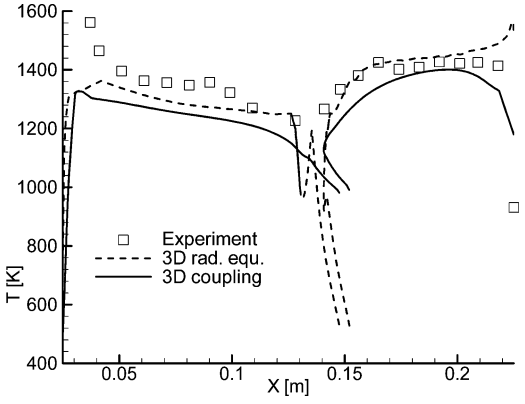

Fig. 33 Closed gap: comparison of surface temperature with experimental data in symmetry plane.

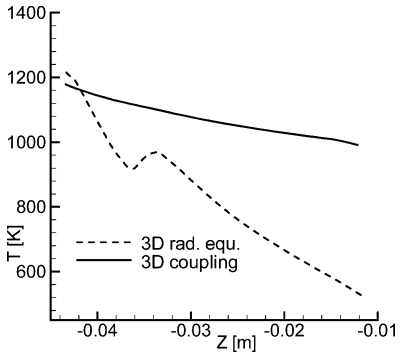

Fig. 34 Closed gap: surface temperature of coupled and uncoupled solutions in symmetry plane (backward gap side, in *z* direction).

below the radiation equilibrium one. The reattachment peak on the gap forward wall is also smoothed. The described phenomena for the backplate is also shown for the side wall in Fig. 31.

Figure 32 shows spanwise temperature comparisons between simulation and experiment. Except for the offset already described, the distributions are well predicted. On the forebody, the temperature is almost constant (lines 1 and 2), whereas on the body flap the temperature increases at the side edges due to the three-dimensional effect, both numerically as well as experimentally.

The behavior of the gap temperature of the coupled three-dimensional solution compared with uncoupled (Fig. 34) matches better with the experiment, which indicates a gap temperature of 1000 K at the bottom (not shown here). Indeed, the slope of the curve is better predicted with the coupled solution. The temperature of the cold-gap bottom increases from 550 to 1000 K, and the local peak is smoothed due to the high-heat conductivity of the C/SiC material to an almost constant temperature gradient inside the gap.

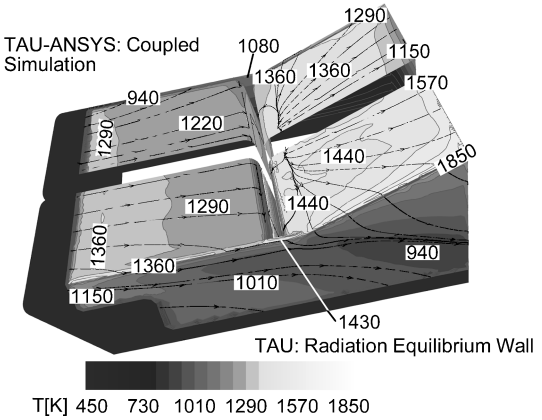

Fig. 35 Open gap, coupled and uncoupled solutions: surface streamlines and temperature distributions.

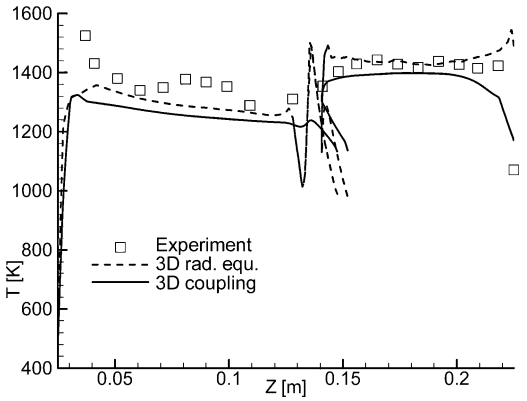

Fig. 36 Open gap: comparison of surface temperature with experimental data in symmetry plane.

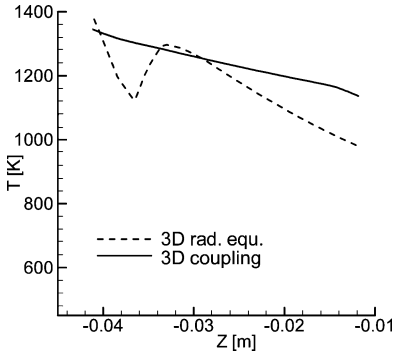

Fig. 37 Open gap: surface temperature of coupled and uncoupled solution in symmetry plane (backward gap side, in *z* direction).

Open-Gap Configuration Simulation

Similar to the closed gap, the temperature peaks at the open-gap configuration are weakened and smoothed (Fig. 35). The global effects of coupling are comparable. The temperature inside the gap is mainly redistributed, and less energy is conducted into the gap region by the C/SiC material. Therefore, the temperature on forebody and body flap are slightly closer to the uncoupled solution (Fig. 36). Except for an offset of approximately 100 K on the forebody and 50 K on the body flap, the simulation shows good agreement with the experiments. Therefore, the flow phenomena are well predicted. Inside the gap (open-gap configuration), the overall temperature was better approximated by the radiation adiabatic wall than for the closed-gap solution: The temperature rises only from 1000 to 1200 K at the gap exit. The slope of the curve inside the gap is well predicted, the temperature of the experiment indicating a temperature of approximately 1150 K with almost constant gradient (not shown here); compare Fig. 37.

Conclusions

In the recent past, the aerothermodynamic problem of deflected control surfaces with highly heated side edges, particularly the hinge line, was extensively simulated as two dimensional by many authors. Although there were differences in computer codes and hypothesis applied, the CFD results always reported a different flow topology than the available experiments with a very large separation bubble. Furthermore, the CFD wall temperatures differed significantly from the experiment, especially for the closed-gap condition, where the differences amounted to up to 500 K. In addition, for the open-gap configuration, the numerical solutions exhibited very large temperature peaks at the gap entry, not shown in the experiments.

No previous CFD solution addressed the numerical error and the crossflow effects on the flow topology. The present study focused, therefore, on these two aspects: the assessment of the numerical error either provided by the solver or the grid used and the assessment of the three-dimensional effects. A numerical coupling tool, consisting of the DLR Navier–Stokes TAU code, the surface interpolation routine MpCCI, and the structural solver ANSYS, was applied. Two- and three-dimensional solutions were obtained for a generic body-flap model, consisting of a C/SiC forebody with an isothermal copper nose, and a body-flap of C/SiC deflected 20 deg, including a gap between them. One angle of attack, 15 deg, and a two gap configurations, that is, closed and open, were computed under hypersonic conditions at $M = 7.3$.

Two-dimensional calculations performed on meshes of different density with and without adaptation have shown that, as the density of points is reduced, the separation length becomes shorter. A similar trend is found with decreasing the numerical dissipation of the codes; that is, the less dissipative a scheme is and the finer the grid, the worse is its two-dimensional solution compared with the experimental solution. The present investigation demonstrated clearly that the main and primary reason for discrepancies between CFD and experimental data is the presence of strong three-dimensional effect. Indeed, the three-dimensional results show that, even if it vanished at the symmetry plane, a strong crossflow takes place over the model surface, reducing dramatically the separation length and increasing the heat fluxes. Also, the investigation confirmed that the material conductivity is the reason for significantly reduced thermal loads observed at the edges of the gap compared to a CFD fluid-alone solution. Indeed, the CFD fluid–structure coupled solutions showed a smooth distribution of temperature at the flap edges and reattachment lines with a significant reduction of heat peaks due to heat conduction into and inside the model. The investigation demonstrates clearly the potential of the coupling tool, by means of which it will be possible to predict the interactions of surface heat flux and internal structural heat conduction accurately. Quantifying the loads on thermal protection systems reliably will increase the overall safety significantly and will allow a reduction of global design margins in critical areas of future space vehicles due to increased local safety.

Acknowledgments

The authors thank Christian Gautier for the calculations during his research study at DLR, German Aerospace Center; Ali Guelhan and Burkard Esser of DLR, German Aerospace Center, Cologne, for the experimental data; and José M. A. Longo for many valuable discussions during this study.

References

[1]Dunlap, P. H., Steinetz, B. M., Curry, D. M., DeMange, J. J., Rivers, H. K., and Hsu, S.-Y., "Investigations of Control Surface Seals for Re-Entry Vehicles," AIAA Paper 2002-3941, July 2002.

[2]Guelhan, A., Esser, B., and Koch, U., "Experimental Investigation of Gap Flows on a Flap Model in the Arc Heated Facility L3K," DLR, German Aerospace Center, Rept. DLR-IB-39113-99C01, Cologne, Germany, Sept. 1999.

[3]Behr, R., and Goergen, J., "CFD Analysis of Gap Flow Phenomena," DaimlerChryslerAerospace, TET-DASA-21-TN-2403, Munich, March 2000.

[4]Mack, A., and Schaefer, R., "Nutzung des unstrukturierten TAU-Codes zur Stroemungs-Struktur Kopplung im Rahmen des DLR-Projektes IMENS," 10. STAB-Workshop, DGLR/STAB, Goettingen, Nov. 2001.

[5]Fruehauf, H.-H., Jufed, F., Fertig, M., and Olawsky, F., "Thermal Loads for the Experimental Vehicle X-38," *Fourth Symposium on Aerothermodynamics for Space Vehicles*, edited by R. A. Harris, ESA SP-487, 2002, pp. 717–723.

[6]Mack, A., and Hannemann, V., "Validation of the Unstructured DLR-TAU-Code for Hypersonic Flows," AIAA Paper 2002-3111, June 2002.

[7]Chen, J., and Mack, A., "Hypersonic Flow Computation over X-38 on Unstructured/Hybrid Meshes," DLR, German Aerospace Center, Rept. DLR-IB 129-2000/17, Brunswick, Germany, Sept. 2000.

[8]Kroll, N., and Radespiel, R., "An Improved Flux Vector Split Discretization Scheme for Viscous Flows," DLR, German Aerospace Center, Rept. DLR-FB 93-53, Brunswick, Germany, 1993.

[9]Wada, Y., and Liou, M.-S., "A Flux Splitting Scheme with High-Resolution and Robustness for Discontinuities," AIAA Paper 94-0083, Jan. 1994.

[10]Macrossan, M. N., "The Equilibrium Flux Method for the Calculation of Flows with Non-Equilibrium Chemical Reactions," *Journal of Computational Physics*, Vol. 80, No. 1, 1989, pp. 204–231.

[11]Galle, M., Gerhold, T., and Evans, J., "Parallel Computation of Turbulent Flows Around Complex Geometries on Hybrid Grids with the DLR-Tau Code," *Parallel Computational Fluid Dynamics*, edited by A. Ecer and D. R. Emerson, North-Holland, Amsterdam, 1999.

[12]Hackenberg, M. G., Post, P., Redler, R., and Steckel, B., "MpCCI, Multidisciplinary Applications and Multigrid," *Proceedings ECCOMAS 2000*, CIMNE, Barcelona, Sept. 2000.

[13]Mack, A., and Schaefer, R., "Flowfield Topology Changes Due to Fluid–Structure Interaction in Hypersonic Flow Using ANSYS and TAU," *New Results in Numerical and Experimental Fluid Mechanics IV*, Vol. 87, Springer, Berlin, 2004, pp. 196–203.

W. Williamson
Associate Editor